

Positron Defect Mapping

A dissertation presented
by

Marcus A. Gagliardi

to

The Department of Physics
in partial fulfillment of the requirements
for the degree of
Doctor of Philosophy
in the subject of

Physics

Idaho State University
September 2008

UMI Number: 3345074

INFORMATION TO USERS

The quality of this reproduction is dependent upon the quality of the copy submitted. Broken or indistinct print, colored or poor quality illustrations and photographs, print bleed-through, substandard margins, and improper alignment can adversely affect reproduction.

In the unlikely event that the author did not send a complete manuscript and there are missing pages, these will be noted. Also, if unauthorized copyright material had to be removed, a note will indicate the deletion.

UMI®

UMI Microform 3345074

Copyright 2009 by ProQuest LLC.

All rights reserved. This microform edition is protected against unauthorized copying under Title 17, United States Code.

ProQuest LLC
789 E. Eisenhower Parkway
PO Box 1346
Ann Arbor, MI 48106-1346

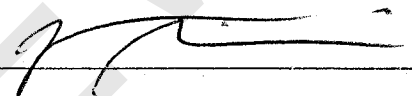
©2008 - Marcus A. Gagliardi

All rights reserved.

PREVIEW

In presenting this thesis in partial fulfillment of the requirements for an advanced degree at Idaho State University, I agree that the Library shall make it freely available for inspection. I further state that permission for extensive copying of my thesis for scholarly purposes may be granted by the Dean of the Graduate School, Dean of my academic division, or by the University Librarian. It is understood that any copying or publication of this thesis for financial gain shall not be allowed without my written permission.

Signature

A handwritten signature in dark ink, appearing to be a stylized 'J' followed by a horizontal line and a small flourish.

Date

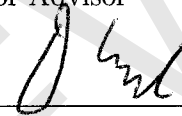
10/14/08

To the Graduate Faculty:


The members of the committee appointed to examine the dissertation of Marcus
A. Gagliardi find it satisfactory and recommend that it be accepted.



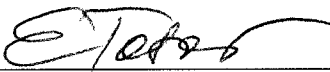
Major Advisor



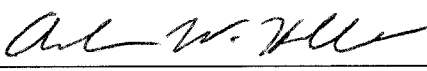
Committee Member



Committee Member



Committee Member



Graduate Faculty Representative

PREVIEW

Thesis advisor
Alan W. Hunt

Author
Marcus A. Gagliardi

Positron Defect Mapping

Abstract

Positron annihilation spectroscopy has been used in the detection of monovacancies as well as dislocations in materials for many years. Using the technique of Doppler broadening, relative defect density measurements were made on several copper coupons that had been annealed as well as shot peened. Due to its nature, shot peening introduces defects such as monovacancies and dislocations into the material. This reproducible technique was used to implant these defects into the copper in order to show that correlations exist between S-parameter and shot peening intensity. Relative defect density maps were produced that allow for verification to be made of different defect density regions. Also, these relative defect density maps can be used to determine if shot peening intensity was uniform over the measured area.

for my mother and my father

PREVIEW

Acknowledgments

The author would like to acknowledge Edward T. E. Reedy and Brian Oborn for their help in the construction of the 6KControl program used extensively in this research. I would also like to acknowledge Anna R. Hoskins for her help and support with the construction and interpellation of experiments and data during the spatial resolution tests. Special thanks go to Kevin Folkman and Brett King for their help and advice in constructing and machining the many devices used for this research.

I would also like to acknowledge my family and friends for all of their help and support over the years. I draw my strength from you. To Paul who has become my brother, who has stood there through the good and the bad and has kept me sane these past few years, thank you for your love and support.

Finally, I would like to give very special thanks my adviser, Dr. Alan W. Hunt. Without your tireless efforts, commitment, trust, and help I am not sure I could have ever made it this far.

Contents

Title Page	ii
Abstract	v
Dedication	vi
Acknowledgments	vii
Table of Contents	viii
List of Figures	x
List of Tables	xvi
1 Introduction	1
1.1 Positrons and Positron Annihilation Spectroscopy	1
1.2 Purpose and Intent	4
2 Fundamentals of positron annihilation spectroscopy	6
2.1 Positron Thermalization	6
2.2 Positron Diffusion	11
2.3 Positron Annihilation and Doppler Broadening	14
2.4 Positron Annihilation Spectroscopy	19
3 The Experimental Setup	27
3.1 Detector and Data Acquisition	27
3.2 Translation Stages and 6KControl Software	29
3.3 Conventional Positron Sources	31
4 Experiments	35
4.1 Determining Proper Experimental Setup and Techniques	35
4.2 Annealed vs. Unannealed Measurements	39
4.3 Bending the Copper Plate	42
4.4 Defect Localization	45
4.5 Calculation and Experimental Determination of System Resolution	47
5 Shot Peening and Defect Density Mapping	55
5.1 Defect Density Measurements of Shot Peened Copper Coupons	55

5.2	Relative Defect Density Measurements of Laser Shock Peened 316L Stainless Steel	62
5.3	Two Dimensional Defect Density Mapping of the Shot Peened Copper Plate	68
6	Conclusions, Future Work, and Applications	75
6.1	Experimental Results	75
6.2	Future Work	77
6.3	Potential Applications	79
	Bibliography	81

PREVIEW

List of Figures

1.1	Figure (a) shows the positron entering the lattice of the material being probed. The material here has no defects and therefore the positron has an equal probability of annihilating with any electron. Figure (b) shows the positron entering the lattice of a material with a point defect. The positron sees this defect as a potential well and in turn has a high probability of being trapped within the defect. Once trapped the positron then will annihilate with a valence electron from one of the surrounding atoms.	2
1.2	These are two 511 keV peaks taken from an annealed and unannealed copper sample. These spectra are normalized to the total number of counts in the peak. The difference in widths are used to illustrate the doppler shift experienced by the annihilating γ -rays due to a material with a relative low defect density (annealed) compared to a material with higher relative defect density (unannealed).	3
2.1	This is a graph of average energy loss calculated from equation 2.7 for copper. The green dashed line represents the radiative stopping power. The red dashed line represents the energy lost due to collisions. It is important to note that this includes the density effect. The solid black line represents the total stopping power, $(-\frac{dE}{dx})$	9
2.2	An approximation of the continuous slowing down approximation of a positron in copper. This figure represents a very close approximation to the average path length traveled by a a positron as it reaches thermalization. In this approximation, the rate of energy loss at every point along the track is assumed to be equal to the same as the total stopping power. Energy-loss fluctuations are neglected.	11

2.3	Basic illustration of a Bloch function. The high regions depict areas where there is a high probability of locating the positron, while the lower valleys are areas with which there is a lower probability for the existence of the positron. It should be noted that this image is only a representation and that the probability of finding a positron in the atomic nuclei can not be negative in value.	13
2.4	Illustration of the trapped positron wave function as calculated in Ni. This illustration is used only to demonstrate how the positron's wave function may vary from diffusion into a trapped state.	14
2.5	Vector diagram of the two γ annihilation in the laboratory frame. The total momentum of the annihilation radiation is denoted as P . The longitudinal and transverse momentums are denoted as P_L and P_T respectively. The angle of deviation from collinearity is denoted by θ and P_1 and P_2 are the measured momentum of the γ -rays.	16
2.6	Doppler broadened 511 keV peak. The areas used for defining the central and wing regions are defined.	20
2.7	Example of a 511 keV peak. The red area indicates the S region (R_b) while the blue area indicates the total peak region (T_b) used for the calculation of the S-parameter in equation 2.21. The green regions are used for the side band subtraction.	21
2.8	Example of a 511 keV peak. The red area indicates the S region, r_o and r_f are the initial and final points of the S region. P_o and P_f are the initial and final points of the peak region. LB and UB represent the lower and upper backgrounds respectively.	22
3.1	The schematic illustrates the internal setup of the HPGe detector inside of the shielded house.	28
3.2	Basic layout of the data acquisition system.	29
3.3	Setup for translation stages and HPGe detector. A) Stepper motor for moving the source onto and off of the sample. B) Motion cart used to move the source. C) This is the source holder. D) Sample that is being inspected. E) This is the detector. F) Lead shield surrounding the detector.	30
3.4	Screen shot of the 6KControl program which allows the user to interface with the translation stages. Using this program the user can communicate in various means to produce a variety of input parameters for the creation of a defect density map.	31
3.5	Diagram of β^+ and γ -ray emissions from the ^{22}Na isotope as it decays to the stable state of ^{22}Ne	32
3.6	Energy spectrum of ^{22}Na in β^+ per 10^6 decays per keV. This spectrum further illustrates the primary and secondary decay channels by which the ^{22}Na may decay.	33

3.7	Energy spectrum of ^{68}Ga in β^+ per 10^6 decays per keV. This spectrum is continuous as compared with the β^+ spectrum from the ^{22}Na	34
4.1	A schematic of the holder for the copper plate. This holder provided the largest surface area from which to sample data. This holder was attached directly to the vertical translation stage which was attached to the horizontal translation stage. This allowed for motion of the sample plate in both x and y axis.	36
4.2	Schematic of the copper plate and the copper coupon with the ^{22}Na sandwiched between them. This diagram depicts the experimental setup used to estimate the sample area measured by the detector system.	37
4.3	This graph shows a single horizontal line of data points taken across the surface of the copper plate while the ^{22}Na source was attached. As the translation stages moved the copper plate in 1 cm intervals, it can clearly be seen when the source is directly in front of the detector. . .	38
4.4	The holder for the copper coupon setup. This holder is attached to the translation stage table. It is positioned via a series of connecting rods and placed as close to the opening of the lead collimator as possible. .	41
4.5	Unannealed (■) versus annealed (●) copper coupons. The change in S-parameter indicates that the annealing process removes defects from the original cold-worked metal.	42
4.6	Defect density map of annealed copper plate. The S-parameter is ~ 0.521 across the surface. The slight shift in the bottom right portion of the image was determined to be an artifact.	43
4.7	Defect density map of the bent copper plate. The S-parameter measurements show the change from the low defect density regions (~ 0.530 at the top and the high defect density region in the center (~ 0.544)).	44
4.8	Defect density map of the copper plate with a piece of plastic adhered to its surface. The square shape was used in order to obtain information on the system resolution.	46
4.9	Defect density map of the copper plate with a plastic piece adhered to its surface in the shape of an "I". The "I" shape was used to obtain information on how the edges and corners would effect the overall system resolution.	47
4.10	A schematic diagram representing the experimental setup. (A) represents the new stepper motor that allows for motion along the z-axis. (B) is a small track that is moved by the stepper motor. The resulting motion allows for the source which is attached to (C) to be placed onto the copper plate (D). Item (E) is the detector while item (F) is the lead shielding surrounding the detector. The collimator is not pictured here but was placed at the end of the detector directly in front of the copper plate.	48

4.11	Initial test to acquire the system resolution. Although the “V” shape can be clearly seen the system was unable to provide a clear example of when the two peaks converged	49
4.12	This defect density map was taken using a translation step size of ~ 0.33 cm. Although 20 data points were taken this was not enough to produce a viable function to calculate the system resolution.	50
4.13	This is a one dimensional defect density map produced by measuring on the copper surface and onto the defect simulation. This output signal is referred to as $g(x)$ and the step size for the translation stages was 0.2 mm.	52
4.14	This is the point spread function which is the derivative of $g(x)$. The line fit to the function is a Gaussian which allows for the FWHM to be calculated and thus the resolution of the system to be determined.	53
4.15	This is the second defect density map, $g_2(x)$. This was used to determine the accuracy of the calculated resolution for the previous experiment. In order to determine what the resolution of the system is a distinction in the peaks must be visible. Here the distinction can be made between the first and second peak indicating that ~ 2 mm is the smallest distance between two defects that can occur and still be distinguishable. Thus a calculated spatial system resolution of ~ 2.2 mm is accurate.	54
5.1	Picture of the four initial shot peened copper coupons. A) is a copper coupon shot peened at 1A. B) is a copper coupon shot peened at 3A. C) is a copper coupon shot peened at 5A. D) is a copper coupon shot peened at 10A. As the intensity of the shot increases so does the amount of damage to the surface of the copper coupon.	57
5.2	S-parameter versus shot peened intensity on the “A” scale. As the shot intensity increases so does the measured S-parameter. The annealed and unannealed S-parameters are included for comparison.	58
5.3	S-parameter versus shot peened intensity on the “A” (●), and “N” (■) scale. There is a difference in S-parameter measurement for the “N” scale versus the “A” scale. However, they both saturate at the same value. The annealed and unannealed S-parameters are included for comparison.	60
5.4	S-parameter versus shot peened intensity on the “A” scale for the 5A and 10A pieces. Each set was measured using both the ^{68}Ge source (■) and the ^{22}Na source (●).	61
5.5	Schematic of laser shock peening technique. This figure describes the method of laser shock peening known as “confined ablation”.	63

5.6	Microhardness test (Vickers) performed on the 316L stainless steel piece after the laser shock peening process. This graph shows the hardness decreasing from $\sim 270 \text{ kg/mm}^2$ to $\sim 190 \text{ kg/mm}^2$ within 2.5 mm of the surface [57].	64
5.7	Slices removed from the original laser shock peened stainless steel coupon. Each side was labeled so that individual S-parameter measurements could be made of each piece. Once complete a graph was constructed to compare the data from figure 5.6 with these measurements.	65
5.8	S-parameter measurements were taken of each side of each piece of 316L stainless steel, as described in figure 5.7 The depths listed here correspond to the approximate depth at which each side of each slice was cut from. The annealed piece of 316L stainless steel is shown here for comparison.	67
5.9	Using data taken from figure 5.6 the hardness ($\text{kg} \cdot \text{mm}^{-2}$) was approximated for each side of each piece of the 316L stainless steel laser shock peened. This graph shows the S-parameter measured versus each piece's corresponding hardness.	68
5.10	Copper plate covers used to ensure that shot peening was only performed on specific areas of the copper plate at the desired intensities. Schematic (a) is the first cover used to shot peen a series of circles at an intensity of 1A. Schematic (b) shows the second cover that was used to shot peen the copper surface at an intensity of 3A. This cover also included a series of 2 mm vertical lines used to measure the spatial resolution of the system. The figure at the bottom of the cover represents the letters "I", "A" and "C". Schematic (c) is the final cover used to shot peen the copper surface at an intensity of 5A.	69
5.11	This figure shows the section of the copper plate that was imaged for this experiment. The circles indicate the regions shot peened at various intensities. The circular regions measured are labeled as to which shot intensity was used on that region.	70
5.12	This is the defect density map of the measured circular area of the copper plate. The step size of the translation stages used to create this map was 2 mm. Clear distinctions can be made between each of the circular regions. Although a slight difference can be seen in the regions that were shot peened at 1A from that shot peened at 3A only a 30 point difference is measurable when comparing the average S-parameter of each region.	71

- 5.13 This figure describes the statistical variation of the S-parameter measurements averaged for the top left 1A circular shot peened region as seen in figure 5.12. The solid horizontal line represents the average S-parameter measured for these data points. It would be expected that $\sim 68\%$ of the data points would be within the average S-parameter, however, this is not the case. 72
- 5.14 Average S-parameter measured for the central 1A shot peened region and the top right 3A shot peened region. The figure shows that the two measurements are distinguishable and outside of error bars. Thus, the higher S-parameter measured for the 3A region shows an area of higher defect density as expected. 73
- 6.1 This is the defect density map of the letters "I", "A", and "C" shot peened onto the copper plate. The step size of the translation stages used to create this map was 2 mm. Although a slight difference can be seen in these three regions, the average S-parameter for each region is ~ 0.55 76

PREVIEW

List of Tables

4.1 FWHM used to calibrate all experimental setups	35
--	----

Chapter 1

Introduction

1.1 Positrons and Positron Annihilation Spectroscopy

Since its prediction by Dirac in the 1920's and its subsequent discovery by Anderson in 1933, many uses have been predicted for the positron [2, 15, 16]. In 1949 S. DeBenedetti et al. discovered that the two γ -rays arising from the annihilation of thermalized positrons in a solid material were not collinear. This phenomenon was attributed to the electron momentum of the annihilating pair. Thus, began a new era of using positrons to probe solid-state materials [12, 54].

When the emitted positron enters a material it will thermalize, typically, within the first few micrometers of the surface [24, 43, 47]. Once thermal equilibrium is reached the positron will annihilate with an electron from the surrounding medium. The dominant annihilation of the positron with the electron leads to two γ -rays. This entire annihilation process will, in general, take place within 100 to 500 picoseconds (ps). If the lattice structure of the material is free of any defects such as dislocations, or point defects as seen in figure 1.1 a, the positron has a larger probability of annihilating with a high momentum core electron. In contrast, if the positron enters a material where monovacancies exist as seen in figure 1.1 b the positron can become trapped in the defect, decreasing the probability of annihilating with high momentum core electrons and hence increasing the probability of annihilating with low momentum valence electrons. Doppler Broadening Spectroscopy, or as it will be

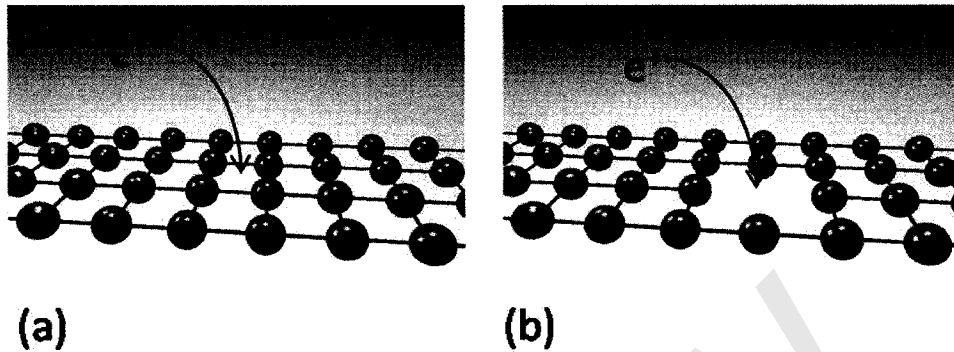


Figure 1.1: Figure (a) shows the positron entering the lattice of the material being probed. The material here has no defects and therefore the positron has an equal probability of annihilating with any electron. Figure (b) shows the positron entering the lattice of a material with a point defect. The positron sees this defect as a potential well and in turn has a high probability of being trapped within the defect. Once trapped the positron then will annihilate with a valence electron from one of the surrounding atoms.

referred to in this text, positron annihilation spectroscopy (PAS), is commonly used for determining which of these two processes takes place.

The positron annihilation spectroscopy process in these experiments was conducted through the use of a high purity germanium (HPGe) detector [38]. The energies of the emitted γ -rays are detected as a peak with an energy of approximately 511 keV. Although more detail will be given later in this text as to the specifics of this measuring method, it is the change in width of this 511 keV peak that is used to distinguish the annihilation of positrons within defects. Figure 1.2 shows the resulting 511 keV annihilation lines as measured by the HPGe detector. The 511 keV line from the annealed copper is broader than that of the manufactured copper. This implies that the momentum of the annihilating electrons measured from the annealed copper is larger than that of the as manufactured copper. Due to the annealing process, defects like mono-vacancies are less prevalent. Therefore, the positrons have a higher probability of annihilating with core electrons than they would if they were in a material with a larger number of defects, such as mono-vacancies. In contrast, the manufactured copper has a large concentration of defects, due to the cold working

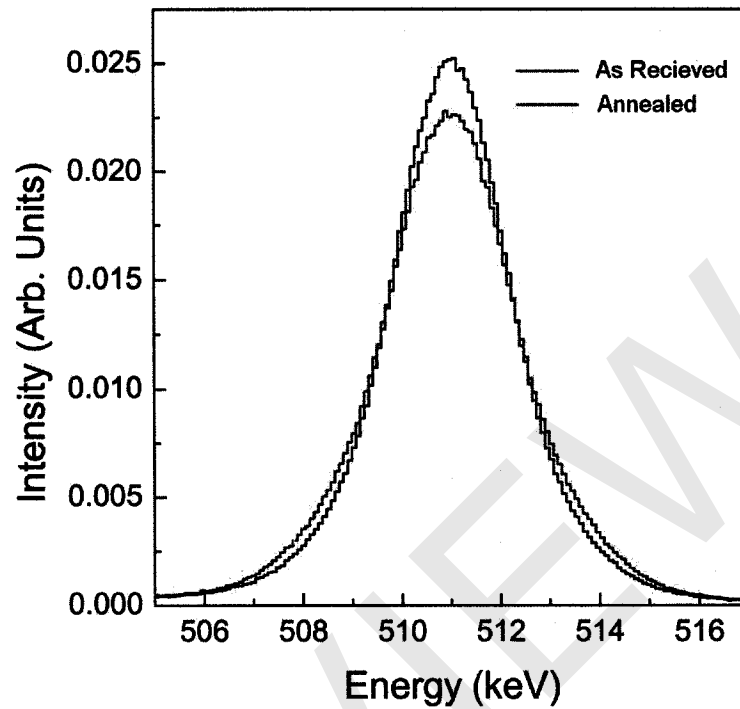


Figure 1.2: These are two 511 keV peaks taken from an annealed and unannealed copper sample. These spectra are normalized to the total number of counts in the peak. The difference in widths are used to illustrate the doppler shift experienced by the annihilating γ -rays due to a material with a relative low defect density (annealed) compared to a material with higher relative defect density (unannealed).

performed on the metal during the manufacturing process. As previously mentioned, positrons interacting with materials that have a larger number of defects will have a higher probability of annihilating with valence electrons, this in turn will cause a narrowing of the 511 keV annihilation line as seen in figure 1.2. Analysis of the 511 keV annihilation lines width allows a measurement of the relative defect densities of the material under test.

1.2 Purpose and Intent

The goal of this doctoral research was to map relative defect densities from a two dimensional surface. Using positron annihilation spectroscopy, measurements of the 511 keV annihilation line width were taken from several points on a copper plate. Each of these data points were measured and reconstructed into a map of location versus relative defect density. The process of conducting these experiments began with the construction of the experimental apparatus. Although alterations were made for later experiments the following description of the system remained unchanged.

This research required a data acquisition and control system. The data acquisition system consisted of several nuclear instrumentation modules as well as data acquisition software a computer control program, and a HPGe. The control system consisted of a series of motion control tables. The details of these systems will be discussed in more detail in Chapter 3.

Two sets of experiments were conducted to test the experimental apparatus. The first set of experiments tested the two-dimensional mapping technique that would be used later for the construction of a relative defect density map. With these experiments the system resolution was calculated. The second set of experiments measured sensitivity to defects. An understanding of the system's sensitivity was paramount in distinguishing variations in the overall defects on the material surface. As discussed in Chapter 4.3 the bending of the copper plate induced a large amount of damage that extended throughout the plate. Hence, a more precise technique was required to create defects.

Shot peening was used to create and obtain well defined regions of relative defect density. Using copper coupons shot at different intensities, reproducible measurements were made of these relative defect densities. Comparison of those relative defect densities made by shot peening to those measurements made of annealed and unannealed pieces provided a scale of shot intensity versus relative defect density. A saturation point was reached in the measurements of the shot peened pieces, where no further variance could be observed between the relative defect densities. This saturation effect agrees with results from S. Saterlie et al. using PAS on shot peened

aluminum [53].

The final set of experiments combined the sensitivity measurement with the mapping techniques. A new annealed copper plate was used and surface regions were shot peened at different intensities. A series of two-dimensional maps were produced in order to distinguish the shape and intensity of relative defect density at each location. It is shown that although defect density maps are relative to each material being used, defect densities of varying intensity can be imaged and distinguished using this technique.

PREVIEW

Chapter 2

Fundamentals of positron annihilation spectroscopy

2.1 Positron Thermalization

Upon entering a solid, energetic positrons rapidly lose energy by several processes until reaching thermal energies. For positrons in copper with energies above ~ 20 MeV, this thermalization process is first dominated by the emission of bremsstrahlung radiation [11, 25]. Since β^+ spectra typically have endpoint energies of ~ 1 MeV, bremsstrahlung production is often negligible. At energies below ~ 20 MeV positron energy loss is dominated by collisions with the electron gas until ~ 20 eV. Below this ionization threshold, positrons lose energy by plasmon creation in metals and interband excitation in semiconductors [35, 37, 39]. Finally, positrons lose energy to phonon interactions below ~ 0.1 eV until the positron reaches thermal energies [35, 37, 39].

At energies down to ~ 20 MeV, energy loss due to bremsstrahlung is dominant and given by

$$-\frac{dE_o}{dx} = N \int_0^1 k \phi_k d\left(\frac{k}{E_o - \mu}\right), \quad (2.1)$$

where E_o is the positrons total energy, N is the atomic number density, k is the photon energy, μ is the rest energy of the electron, and ϕ_k is the bremsstrahlung

cross section. Performing the integration, equation 2.1 can be written as

$$-\left(\frac{dE_o}{dx}\right)_{rad} = NE_o\phi_{rad}, \quad (2.2)$$

where ϕ_{rad} is the cross section for the energy lost by radiation, is related to equation 2.1, and takes the form of,

$$\phi_{rad} = \frac{1}{E_o} \int_0^1 k\phi_k d\left(\frac{k}{E_o - \mu}\right). \quad (2.3)$$

After performing the integration equation 2.3 takes the form

$$\begin{aligned} \phi_{rad} = \bar{\phi} & \left[\frac{12E_o^2 + 4\mu^2}{3E_op_o} \log \frac{E_o + p_o}{\mu} - \frac{(8E_o + 6p_o)\mu^2}{3E_op_o^2} \left(\log \frac{E_o + p_o}{\mu} \right)^2 \right. \\ & \left. - \frac{4}{3} + \frac{2\mu^2}{E_op_o} F\left(\frac{2p_o(E_o + p_o)}{\mu^2}\right) \right], \end{aligned} \quad (2.4)$$

where p_o is the momentum of the positron; $\bar{\phi} = \frac{Z^2 r_o^2}{137}$; and F is a function defined by the integral

$$F(x) = \int_0^x \frac{\log(1+y)}{y} dy \quad [25].$$

Once the positron's energy has fallen below ~ 20 MeV the process of ionization dominates as the main cause of energy loss. As the positron moves through the material its energy is transferred to the electrons, which can also cause ionization. Energy loss calculations were first conducted by Bohr using classical theory [6]. These calculations have also been performed using quantum mechanics. The formula for energy lost by the positron traveling with velocity $v = c\beta$ is

$$-\left(\frac{dE}{dx}\right)_{coll} = NZ\phi_o\mu \frac{3}{4} \frac{e^2}{\beta^2} \left[\log \frac{2\mu\beta^2 W_m}{I^2 Z^2 (1 - \beta^2)} - 2\beta^2 \right], \quad (2.5)$$

where ϕ_o is $\left(\frac{8\pi}{3}\right) r_o^2$, e is the charge of the positron, Z is the atomic number, and I is the average ionization energy, which varies for elements of different types. W_m is the maximum energy that can be transferred to a free electron by the positron. For the case of the positron W_m is $\frac{1}{2}(E - \mu)$.

The energy loss equation for positrons with non-relativistic energies ($E - \mu \equiv T \ll \mu$) is

$$-\left(\frac{dE}{dx}\right)_{coll} = NZ\phi_o\mu \frac{3}{4} \frac{\mu}{T} \left[\log \frac{T}{IZ\sqrt{2}} + \frac{1}{2} \right], \quad (2.6)$$